Characterization of mesoporous nanocrystalline TiO$_2$ photocatalysts synthesized via a sol-solvothermal process at a low temperature

Ling Wu, Jimmy C. Yu*, Xinchen Wang, Lizhi Zhang, Jiaguo Yu

Department of Chemistry, The Chinese University of Hong Kong, Shatin, New Territories, Hong Kong, China

Abstract

Nanocrystalline TiO$_2$ samples with mesoporous structure were prepared via a solvothermal treatment of surfactant-stabilized TiO$_2$ sols. The samples were obtained from media of different acidities including nitric acid, deionized water, and ammonia (denoted as HT-1, HT-2 and HT-3, respectively). These samples were characterized by X-ray diffraction (XRD), transmission electron microscopy (TEM), N$_2$-sorption (BET surface area), micro-Raman spectroscopy, infrared absorption spectroscopy (FT-IR) and X-ray photoelectron spectroscopy (XPS). The photocatalytic activities of the samples were tested by the self-photosensitized degradation of an azo dye, Mordant Yellow 10 (MY), in aqueous solution under visible light irradiation. The results reveal that all three samples have high surface area and are pure anatase phase. The sample prepared in nitric acid medium possesses the most ideal mesoporous structure and also exhibits a blue shift in the Raman spectrum. All three samples show much higher photocatalytic activity than the commercial P-25. The activity order of the three samples is HT-1>HT-2>HT-3.
© 2004 Elsevier Inc. All rights reserved.

Keywords: Sol-solvothermal synthesis; Mesoporous TiO$_2$; Dye self-sensitization; Photocatalytic activity

1. Introduction

Since the discovery of photocatalytic water splitting on TiO$_2$ single-crystal electrodes by Fujishima and Honda in 1972 [1], titanium dioxide has been intensively investigated as photocatalysts in the fields of solar energy conversion, water splitting and environmental purification [2–10]. Nanocrystalline TiO$_2$ has high photocatalytic efficiency because of its unique properties conferred by the very small physical dimensions [11–14]. The large specific surface area and the high volume fraction of atoms located both on the surface and at the grain boundaries result in an increased surface energy. Therefore, the surface of nanocrystalline TiO$_2$ provides an active substrate for catalysis. In this respect, nanocrystalline TiO$_2$ particles with a mesoporous structural network will be more promising because light

harvesting can be further enhanced due to the enlarged surface area and multiple scattering. They can also facilitate better accessibility of reactants to the catalysts [15].

Mesoporous TiO$_2$ is often prepared by the sol–gel method involving a co-assembly of titanium precursors and surfactants in the presence of stabilizing agents [15–23]. This is followed by thermal treatment or solvent extraction for surfactant elimination, framework solidification and pore-surface liberation. However, most of the mesoporous TiO$_2$ produced are typically amorphous or semicrystalline in nature. Although further heating at high-temperatures would activate the material into highly crystalline structure, excessive thermal energy often leads to the collapse of mesoporous frameworks accompanied by loss of surface area and pore volume [24,25]. Therefore, it is still a challenge to fabricate mesoporous TiO$_2$ with crystalline framework via a low-temperature process. Several approaches, such as hydrothermal treatment [26] and ultrasound-aided

*Corresponding author. Fax: +852 2603 5057.
E-mail address: jimyu@cuhk.edu.hk (J.C. Yu).

synthesis [27], have been proposed to synthesize crystalline mesoporous TiO_2. Here, we report a low-temperature hybrid approach of sol–gel and solvothermal to produce crystalline mesoporous TiO_2 without the requirement of post thermal treatment. In this approach, a homogenous micelle-stabilized-TiO_2 sol solution is first synthesized by the hydrolysis and co-condensation of a titanium alkoxide in the presence of a surfactant and a stabilizing agent. Subsequent solvothermal treatment of the sol solution removes the surfactant and transfers the amorphous TiO_2 into crystalline nanoparticles [28–30]. Finally, the TiO_2 nanocrystals then assemble together into a mesoporous network.

Mordant Yellow 10 (MY) is non-biodegradable and can accumulate in the aquatic system becoming a major source of contamination [31]. Much effort has been made for the self-sensitized degradation of these dye pollutants [32–42]. Most of these studies were focused on the mechanism of photosensitized destruction of azo-dyes using commercial TiO_2 (Degussa P-25) as a model photocatalyst. It is established that the dye self-sensitized oxidation under visible light irradiation is initiated by the injection of electrons from LOMO of light-activated dye to conduction band of TiO_2. The injected electrons at the particle surface are trapped by surface-adsorbed O_2, yielding very reactive radials such as $O_2^- \bullet$, $HOO\bullet$, and $HO\bullet$ that lead to their degradation and ultimately to their completely mineralization to CO_2. Although TiO_2 is not directly excited by irradiation during this process, the efficiency of dye-degradation is still believed to be related to the physicochemical properties of TiO_2. These properties, including size, shape and surface area, are strongly dependent on preparation methods. Very recently, we reported several preparation routes of mesoporous nanocrystalline TiO_2 powders and thin-films [25,27,43–46], which show high activities in gas–solid photocatalytic systems under UV illumination. In the present work, the application of the large-surface-area mesoporous nanocrystaline TiO_2 has been extended to liquid–solid systems, where visible light was employed to induce the self-sensitized degradation of azo dye. Photocatalytic activity tests reveal that such mesoporous nanocrystalline TiO_2 is a superior photocatalyst to P-25. The effects of acid-base additives (nitric acid, deionized water, and ammonia) on the mesoporous structure and the photocatalytic activity of samples are also described.

2. Experimental

2.1. Synthesis

All reagents were purchased from Aldrich. Titanium tetraisopropoxide (TTIP) was used as a titanium precursor. A surfactant Pluronics triblock copolymer $(HO(CH_2CH_2O)_{20}(CH_2CH-(CH_3)O)_{70}(CH_2CH_2O)_{20}H$, P123, MW = 5800) was used as the structural-directing agent, and a complexing agent acetylacetone (Hacac) was used to control the hydrolysis and condensation reactions of the precursor. In a typical synthesis, titanium tetraisopropoxide was added dropwise to an absolute ethanol solution of P123 and Hacac under stirring. A 10% nitric acid was then added to the mixture. The molar ratios of the ingredients were: titanium precursor/P123/acac/10% nitric acid/ ethanol = 1:0.05:0.5:1.5:43. The final solution (pH is about 3) was stirred for 24 h at room temperature. The resulting sol was placed in a 100 mL Teflon-lined stainless steel autoclave, which was then put in an oven for solvothermal treatment at 80 °C for 18 h and then 150 °C for 20 h. The white slurry obtained was centrifuged and washed with ethanol and water. Finally the sample was dried in a vacuum oven at 100 °C under vacuum. This sample was denoted as sample HT-1. Sample HT-2 and HT-3 were prepared by the same procedure, but the nitric acid was replaced by deionized water and 10% ammonia, respectively. The pH values of the resulting solutions were 6 and 9.

2.2. Characterization

The Brunauer–Emmett–Teller (BET) surface area (S_{BET}) and pore size distribution were determined by using a Micromeritics ASAP 2010 nitrogen adsorption apparatus. All the samples were degassed at 180 °C prior to BET measurements. Wide-angle XRD patterns were obtained on a Bruker D8 Advance X-ray diffractometer with Cu-$K\alpha$ radiation at a scanning rate of $0.02°\ 2\theta\ S^{-1}$. The accelerating voltage and the applied current were 40 kV and 40 mA, respectively. The crystallite size was calculated from X-ray line broadening by the Scherer equation: $D = 0.89\lambda/\beta\cos\theta$, where D is the crystal size in nm, λ is the Cu-$K\alpha$ wavelength (0.15406), β is the half-width of the peak in rad, and θ is the corresponding diffraction angle. Low-angle XRD patterns were collected on the same diffractometer in $\theta-\theta$ mode at a scanning rate of $0.002°\ 2\theta\ S^{-1}$. Raman spectra of the powder samples on a glass slide were measured using a Renishaw 1000 micro-Raman system. Objectives of 50 times magnification were selected. The excitation source was an Argon ion laser operating at 514.5 nm with an output power of 20 mW. Infrared (IR) spectra of the samples mixed with KBr were recorded on a Nicolet Magna 560 FTIR spectrometer at a resolution of $4\ cm^{-1}$. The concentration of the samples was kept at around 0.5%. TEM images were taken on a Philips CM-120 electron microscopy instrument. HRTEM images were taken on a high-resolution transmission electron microscopy system (JEOL2010F) at an accelerating voltage of 200 kV. A suspension in ethanol was

sonicated, and a drop was dropped on the support film. The powder particles were then supported on a carbon film coated on a 3 mm diameter fine-mesh copper grid. X-ray photoelectron spectroscopy (XPS) measurements were done with a PHI Quantum 2000 XPS system with a monochromatic Al-$K\alpha$ source and a charge neutralizer; all the binding energies were referenced to the C1 s peak at 284.8 eV of the surface adventitious carbon.

2.3. Photocatalytic activity test

Photocatalytic activities of the samples were measured by the decomposition of MY in an aqueous solution. Air was bubbled into the solution throughout the entire experiment. A 300 W tungsten halogen lamp was positioned inside a cylindrical Pyrex vessel and surrounded by a circulating water jacket (Pyrex) to cool it. A cutoff filter was placed outside the Pyrex jacket to completely remove all wavelengths less than 400 nm to secure the irradiation with visible light only. 0.1 g of photocatalyst was suspended in a 100 mL aqueous solution of 1.5×10^{-4} M MY. Prior to irradiation, the suspensions were magnetically stirred in the dark for 1 h to ensure the establishment of an adsorption/desorption equilibrium among the photocatalyst, MY and atmospheric oxygen. At given irradiation time intervals, 4 mL of the suspensions were collected, then centrifuged, and filtered through a Millipore filter (pore size, 0.22 in) to remove the photocatalyst particles. The degraded MY solutions were analyzed by a Varian Cary 100 Scan UV-Visible spectrophotometer and the absorption peak at 355 nm was monitored. The structure of MY is shown below:

$$NaO_3S - \langle \ \rangle - N = N - \langle \ \rangle - OH \atop COONa$$
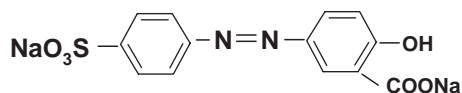
C. I. Mordant Yellow 10 (MY)

3. Results and discussion

3.1. Nitrogen adsorption and XRD analysis

Fig. 1 shows the N_2-sorption isotherms (inset) of the samples with their corresponding pore size distribution curves calculated from the desorption branch of the N_2-sorption isotherms by the BJH (Barrett–Joyner–Halenda) method. Clear hysteresis loops at high relative pressure are observed. The sharp decline in the desorption curves is an indication of mesoporosity. The pore-size distribution plot shows that HT-1 exhibits a mean pore diameter of 4.4 nm with a narrow distribution (FWHM = 2 nm). This narrow pore size distribution is also observed for HT-2, but with a slightly increased pore size (6.7 nm, FWHM = 5 nm). However, sample HT-3 prepared in the ammonia medium has a much larger average pore size of 10.6 nm and a broad pore size distribution (FWHM = 10 nm). The BET surface area, pore size, and pore volume of the prepared samples are summarized in Table 1. The surface areas of HT-1, HT-2 and HT-3 are 205, 185 and 116 $m^2 g^{-1}$, respectively. These, together with the pore size distributions, indicate that acid-base medium significantly affects the mesoporous structure properties of the samples. The mesoporous TiO_2 prepared using the sol-solvothermal method have high surface area and pore volume, which provides more surface active sites and pore-channels for the chemisorption and diffusion of reactants.

The mesoporous structure of the samples is also confirmed by the low angle XRD patterns. As shown in Fig. 2b, only one broad peak at about 1° is observed for HT-1, indicating the existence of worm-like mesoporous structure in the sample. For HT-2 and HT-3, the peak becomes broad and weak, and shifts to a higher 2θ angle. This means that the mesoporous structure is poorly formed in the media of higher pH. These results are consistent with literature reports that mesoporous TiO_2 is better formed in acidic medium [20,46]. The wide XRD patterns (Fig. 2a) of the three samples give five distinctive TiO_2 peaks at 25.3°, 37.9°, 48.0°, 54.6° and 62.8°, corresponding to anatase (101), (103, 004 and 112), (200), (105 and 211), (204) crystal planes (JCPDS 21-1272), respectively. These results indicate that all samples prepared by the sol-solvothermal method are pure anatase, the most photocatalytically active form of TiO_2. The average crystallite sizes estimated form the FWHM of the (101) peak are 7.0, 7.4 and 12.3 nm for HT-1, HT-2 and HT-3, respectively.

3.2. Spectroscopy analysis

Raman spectra were recorded to identify the phase composition. A comparison of Raman spectroscopy with X-ray diffraction can be used to estimate the difference between the surface and bulk compositions of TiO_2 powders because an exciting energy in the near IR region is less penetrating than X-rays [47]. There are three phase structures for titanium dioxide. Anatase is tetragonal ($I41/amd$) with four formula units per unit cell and six Raman active modes ($A_{1g} + 2B_{1g} + 3E_g$). Rutile (tetragonal, $P42/mnm$) has two units and four Raman active modes ($A_{1g} + B_{1g} + B_{2g} + E_g$). Brookite is orthorhombic (Pcab) with eight formula units per unit cell, and it shows 36 Raman active modes ($9A_{1g} + 9B_{1g} + 9B_{2g} + 9B_{3g}$) [48].

The Raman spectra of the samples are shown in Fig. 3a. Five peaks can be observed: a sharp peak at 146 cm^{-1} (but 144 cm^{-1} for HT-3), three wide mid-
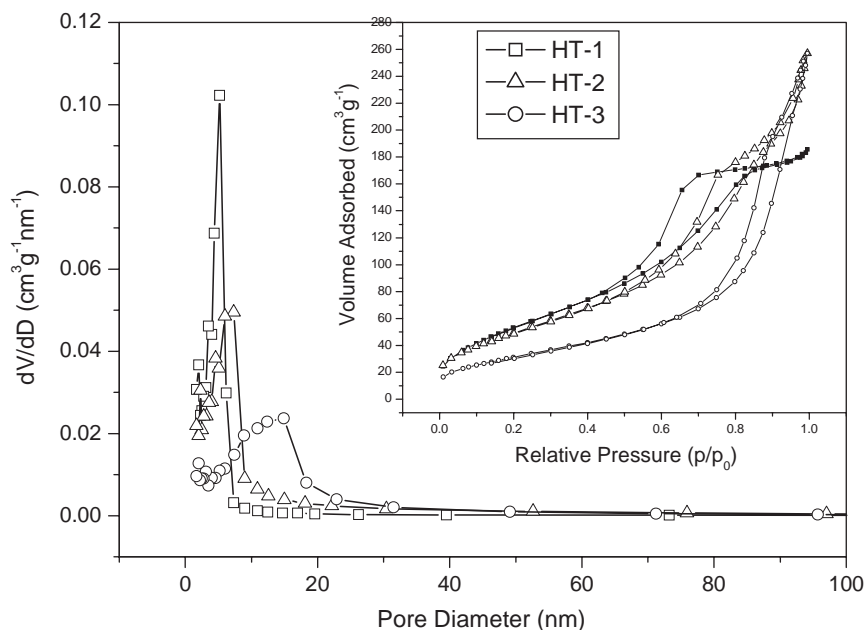
Fig. 1. N_2 adsorption–desorption isotherms (inset) and BJH pore size distributions; □: sample HT-1, Δ: sample HT-2, ○: sample HT-3.

Table 1
Summary of the physicochemical properties of the prepared samples

Sample	pH	$S_{BET}(m^2 g^{-1})^a$	Total pore volume[b] $(cm^3 g^{-1})$	Mean pore size[c] (nm)	Crystal size[d] (nm)
HT-1	3	205	0.28	4.4	7.0
HT-2	6	185	0.34	6.7	7.4
HT-3	9	116	0.35	10.6	12.3

[a]BET surface area calculated from the linear part of the BET plot.
[b]Single point total pore volume of pores at $P/P_0 = 0.97$.
[c]Estimated using the BJH desorption branch of the isotherm.
[d]Calculated by the Scherrer equation.

intensity peaks at 396, 514, and $638\,cm^{-1}$ and a weak peak at $198\,cm^{-1}$. The three bands at 638, 198, and $146\,cm^{-1}$ are assigned to the E_g modes and the band at $396\,cm^{-1}$ to the B_{1g} mode of the TiO_2 anatase phase. The band at $514\,cm^{-1}$ is a doublet of A_{1g} and B_{1g} modes. These observations are similar to those reported in the literature [48,49]. From Fig. 3b, it can clearly be seen that the Raman peaks of HT-1 and HT-2 at $146\,cm^{-1}$ are blue shifted by $2\,cm^{-1}$ as compared with that of HT-3, which is identical to the Raman band of bulk TiO_2.

To examine whether the template was completely removed and to detect the presence of surface species in the prepared samples, FTIR spectra of the samples were recorded in the range of $900–4000\,cm^{-1}$. Fig. 4 shows that two absorption peaks are present, one at $3420\,cm^{-1}$ and the other at $1630\,cm^{-1}$. These correspond to the surface-adsorbed water and oxygen species [50,51]. Small characteristic CO_2 peaks at 2360 and $2337\,cm^{-1}$ are also observed. There is no trace of residual organic species, nitrate or ammonia ions, indicating that the

prepared mesoporous TiO_2 samples are free of impurity. The three spectra are virtually identical.

3.3. TEM and HRTEM images

The TEM and HRTEM images of the three samples are shown in Fig. 5. The representative TEM images (Fig. 5a, c and e) of HT-1, HT-2, and HT-3 reveal that the samples are mesoporous without a long-range order. The mesoporosity is mainly due to the interparticle porosity. These are consistent with the nitrogen adsorption and low-angle XRD results. The average diameters of the particles, estimated from the TEM images of the three samples, are in good agreement with that calculated from XRD patterns using the Scherrer equation. The selected area electron diffraction patterns in the inset of Fig. 5a, c and e also confirm that the three mesoporous TiO_2 samples are polycrystalline anatase. Fig. 5b, d and f are the corresponding HRTEM images of the three mesoporous TiO_2 samples. They show clear
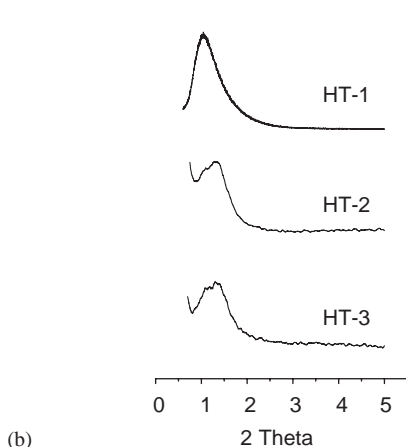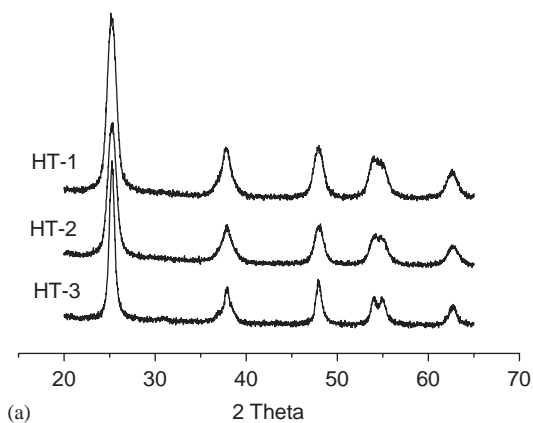
Fig. 2. Wide angle (a) and low angle (b) XRD patterns of HT-1, HT-2 and HT-3.

lattice fringes, which allow for the identification of crystallographic spacing. The fringes of $d = 0.34$ nm match that of the (101) crystallographic plane of anatase. Based on the above results, it is evident that nanocrystalline TiO_2 with wormhole mesoporous structure have been successfully prepared by the sol-solvothermal method. Such wormhole structure with three-dimensionally interconnected but aperiodic pore channels would facilitate the accessibility of reactants to the active sites within the mesoarchitecture [52–54]. This is an attractive feature for heterogeneous catalysis.

3.4. XPS spectroscopy

X-ray photoelectron spectroscopy (XPS) measurements were carried out to determine the surface chemical composition and the oxidation states of the elements in the samples. Fig. 6a shows the XPS survey spectra of the TiO_2 samples. It can be observed that all three samples contain only Ti, O, and C elements. The photoelectron peak for Ti $2p$ appears clearly at a binding energy 458.7 eV, O $1s$ at 530 eV and C $1s$ at 284.8 eV. The peak positions are in agreement with the literature values [55]. Fig. 6b shows the high-resolution
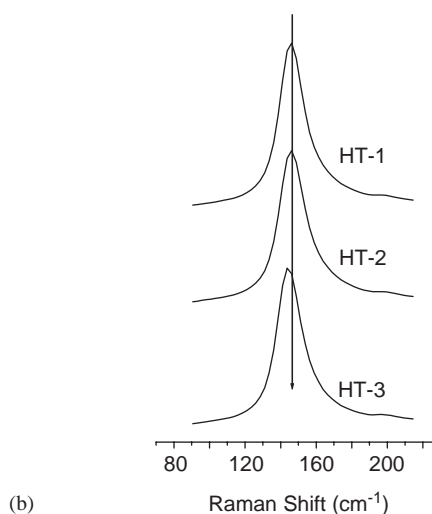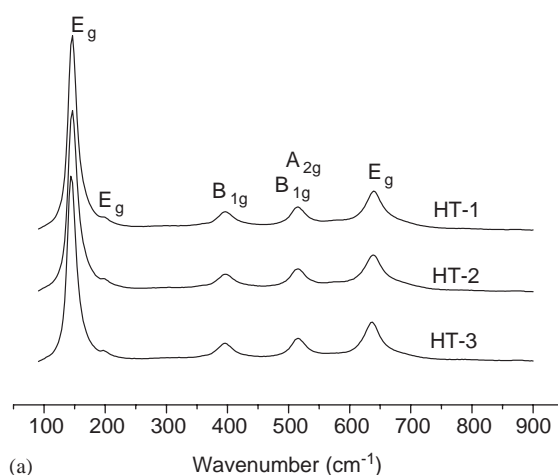

Fig. 3. (a) Micro-Raman spectra of HT-1, HT-2 and HT-3; (b) the enlarged patterns over the range of 80–220 wavenumbers.
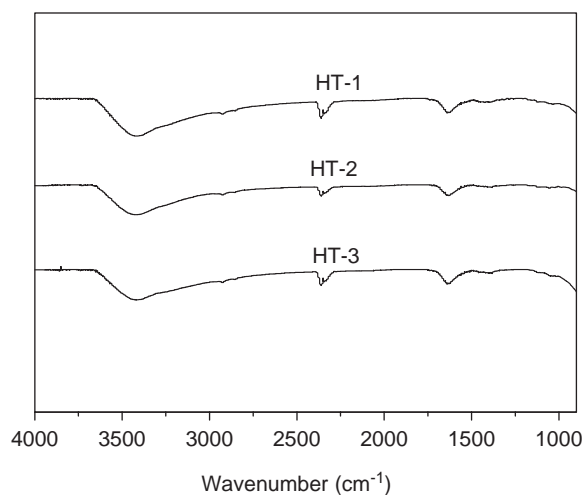

Fig. 4. FT-IR spectra of HT-1, HT-2 and HT-3.

XPS spectra of Ti $2p$. The spin–orbit components ($2p3/2$ and $2p1/2$) of the Ti $2p$ peak are well deconvoluted by two curves at approximately 458.7 and 464.5 eV,
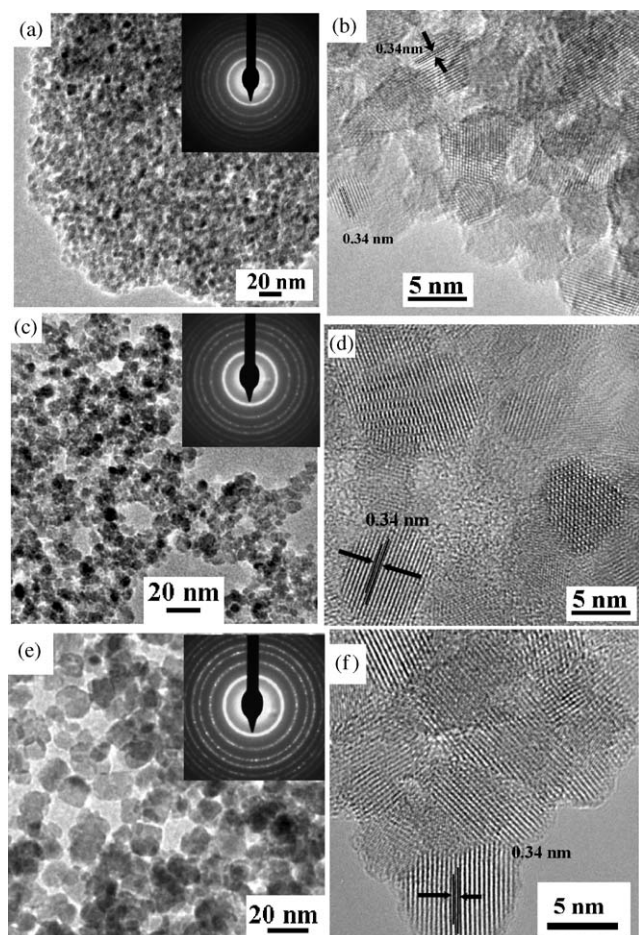
Fig. 5. TEM and HRTEM images: (a) and (b) for HT-1, (c) and (d) for HT-2, (e) and (f) for HT-3. Insets are the corresponding electron diffraction patterns.

corresponding to Ti^{4+} in a tetragonal structure, consistent with that of TiO_2 powders. Fig. 6c shows the high-resolution XPS spectra of O1s of the three samples. The regions of XPS spectra are composed of a narrow peak with a binding energy of ca. 530.0 eV and a broad peak with a binding energy of ca. 531.1 eV. The peaks with 530.0 and 531.1 eV can be respectively attributed to the Ti–O in TiO_2 and hydroxyl groups chemisorbed on the surface of the samples [45,56]. The contributions of OH groups in O1s on the three samples are about 25%. We may thus conclude that the three samples prepared by the sol-solvothermal method at pH values of 3, 6, 9 possess almost the same amounts of surface hydroxyl groups.

3.5. Photocatalytic activity

Photocatalytic activity tests were conducted by the self-sensitized degradation of azo dye MY in aqueous solution under visible light irradiation. Fig. 7a shows the UV-VIS spectra of MY in the present of sample HT-1. MY shows a maximum absorption at 355 nm. The absorption peak gradually diminishes upon the visible light irradiation, illustrating the MY degradation. The concentrations of MY with irradiation time for the three samples and P-25 are shown in Fig. 7b. It is clearly observed that all three samples possess higher photocatalytic activity than P-25. This indicates that the activities of the mesoporous TiO_2 samples prepared by the sol-solvothermal route are superior to that of the commercial TiO_2 P-25 in the dye self-sensitized degradation. HT-1 is obviously the most
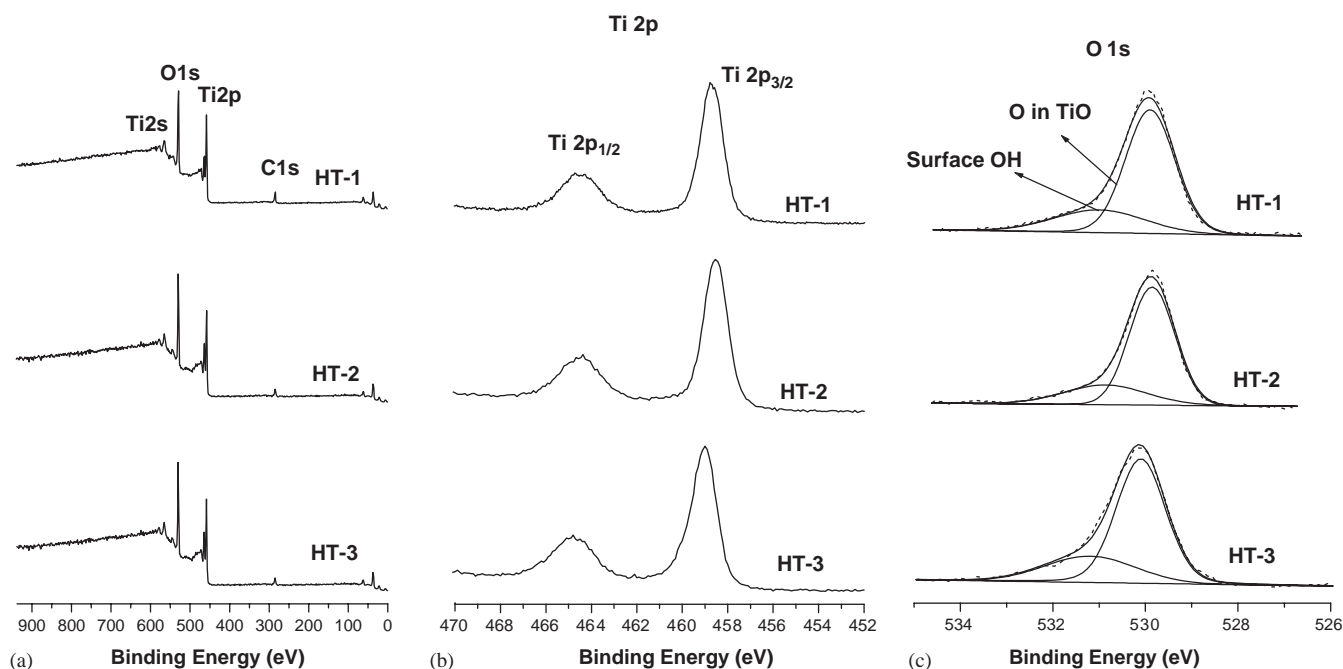

Fig. 6. XPS and high-resolution XPS spectra of HT-1, HT-2 and HT-3: (a) survey, (b) titanium, (c) oxygen.
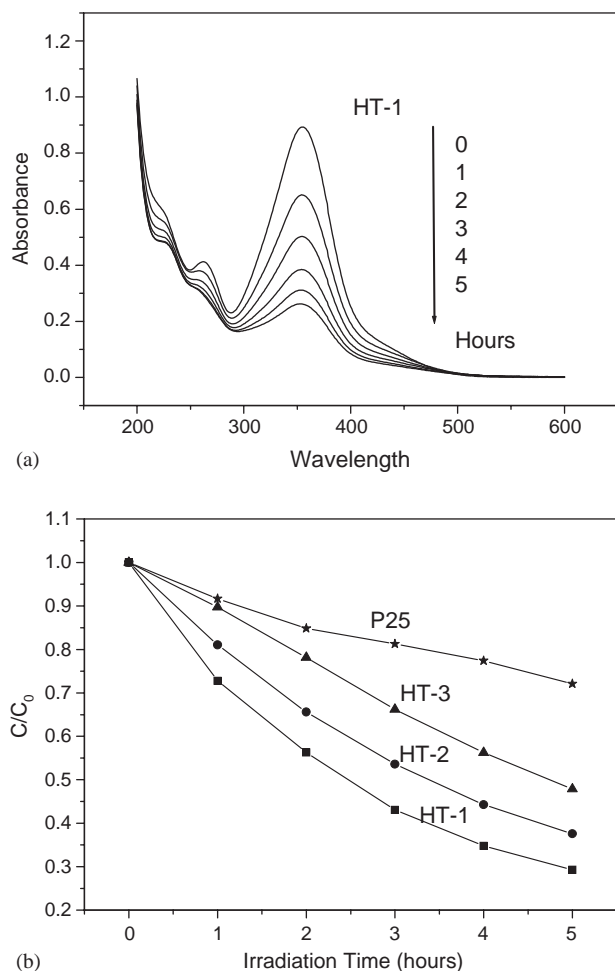
(a)

(b)

Fig. 7. (a) Temporal absorption spectral patterns of MY during the photodegradation process for HT-1, (b) MY reduction in UV-vis absorption spectra at 355 nm as a function of visible-light irradiation time in the prepared samples and P-25.
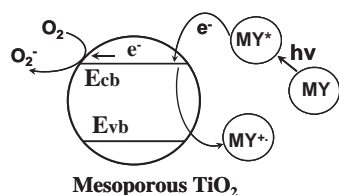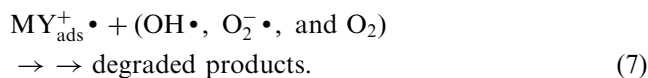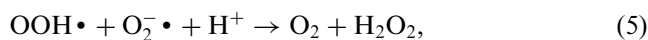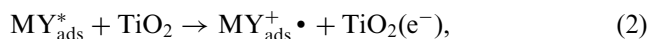

Mesoporous TiO$_2$

Fig. 8. Electron-transfer processes subsequent to excitation of MY.

active sample, and the order of photocatalytic activities is HT-1 > HT-2 > HT-3.

As shown in Fig. 8, the mechanism of the dye self-sensitization degradation under visible light radiation is different from that under UV illumination [32–42]. The valence electrons of TiO$_2$ are not excited by visible light as TiO$_2$ has an absorption threshold of 385 nm. Upon visible light illumination, the chemisorbed MY dye is excited to specific singlet or triplet states (MY$_{ads}$*). Charge is then injected from the singlet or triplet excited states of the dye into the conduction band of the

mesoporous TiO$_2$, whereas the dye is converted to its cationic radical (MY$_{ads}^+\bullet$). The injected electron, TiO$_2$(e$^-$), can reduce surface chemisorbed oxidants, usually O$_2$, to yield strong oxidizing species (such as O$_2^-\bullet$, HO$_2\bullet$, OH$\bullet$ and so on). These radicals can destroy the organic pollutants by photooxidation (Eqs. (1)–(7)). Even though TiO$_2$ itself is not excited in this process, it still plays an important role in electron-transfer and surface chemisorption:

$$MY_{ads} + h\nu \rightarrow MY_{ads}^*, \tag{1}$$

$$MY_{ads}^* + TiO_2 \rightarrow MY_{ads}^+\bullet + TiO_2(e^-), \tag{2}$$

$$TiO_2(e_{cb}^-) + O_2 \rightarrow O_2^-\bullet, \tag{3}$$

$$O_2^-\bullet + H^+ \rightarrow OOH\bullet, \tag{4}$$

$$OOH\bullet + O_2^-\bullet + H^+ \rightarrow O_2 + H_2O_2, \tag{5}$$

$$H_2O_2 + O_2^-\bullet \rightarrow OH\bullet + OH^- + O_2, \tag{6}$$

$$MY_{ads}^+\bullet + (OH\bullet,\ O_2^-\bullet,\ and\ O_2)$$
$$\rightarrow \rightarrow degraded\ products. \tag{7}$$

The three samples prepared in different acidic levels have the same phase structure and surface adsorbed oxygen species, but different surface area and particle size. Therefore, the difference in the activity of the mesoporous TiO$_2$ samples is related to their surface areas and particle sizes. Small particle size not only produces high surface area but also shortens the route on which an electron from the conduction band of the mesoporous TiO$_2$ migrates to its surface. Moreover, a high surface area of the mesoporous TiO$_2$ can provide more active sites and adsorb more reactive species. Since the sample HT-1 has the highest surface area and the smallest crystallite size among the three samples, it exhibits the highest photocatalytic activity.

4. Conclusions

Mesoporous nanocrystalline TiO$_2$ photocatalysts have been prepared via a sol-solvothermal route. The characterization results show that mesoporous structures of the prepared samples consist of interparticle porosity and are most effectively formed in the acidic medium. The mesoporous TiO$_2$ samples also exhibit much higher photocatalytic activities than the commercial P-25 in the self-sensitized degradation of azo dye MY in aqueous solution under visible light irradiation.

Acknowledgments

References

[1] K. Honda, A. Fujishima, Nature 238 (1972) 37.
[2] M.R. Hoffmann, S.T. Martin, W. Choi, D.W. Bahnemann, Chem. Rev. 95 (1995) 69.
[3] A. Fujishima, T.N. Rao, D.A. Tryk, J. Photochem. Photobiol. C 1 (2000) 1.
[4] L. Linsebigler, G. Lu, J.T. Yates Jr., Chem. Rev. 95 (1995) 735.
[5] A. Fujishima, K. Hashimoto, T. Watanabe, Photocatalysis Fundamentals and Applications, first ed., BKC, Tokyo, 1999.
[6] M. Kaneko, I. Okura, Photocatalysis, Science and Technology, Springer, Berlin, 2002.
[7] N. Serpone, E. Pelizzetti, Photocatalysis: Fundamentals and Applications, Wiley, New York, 1989.
[8] D.F. Ollis, H. Al-Ekabi, Photocatalytic Purification and Treatment of Water and Air, Elsevier, Amsterdam, 1993.
[9] M.A. Fox, M.T. Dulay, Chem. Rev. 93 (1993) 341.
[10] A. Mills, R.H. Davies, D. Worsley, Chem. Soc. Rev. 22 (1993) 417.
[11] A. Hagfeldt, M. Gratzel, Chem. Rev. 95 (1995) 49.
[12] Z. Zhang, C.C. Wang, R. Zakaria, J.Y. Ying, J. Phys. Chem. 102 (1998) 10871.
[13] L. Yeung, S.T. Yau, A.J. Maira, J.M. Coronado, J. Soria, P.L. Yue, J. Catal. 219 (2003) 107.
[14] C.B. Almquist, P. Biswas, J. Catal. 212 (2002) 145.
[15] D.M. Antonelli, J.Y. Ying, Angew. Chem. Int. Ed. Engl. 34 (1995) 2014.
[16] P. Yang, D. Zhao, D.I. Margoles, B.F. Chmelka, G.D. Stucky, Nature 396 (1998) 152.
[17] P. Yang, D. Zhao, D.I. Margoles, B.F. Chmelka, G.D. Stucky, Chem. Mater. 11 (1999) 2813.
[18] E.L. Crepaldi, G.J.A.A. Soler-Illia, D. Crosso, F. Cagnol, F. Ribot, C. Sanchez, J. Am. Chem. Soc. 125 (2003) 9770.
[19] H. Fujii, M. Ohtaki, K. Eguchi, J. Am. Chem. Soc. 120 (1998) 6832.
[20] S.Y. Choi, M. Mamak, N. Coombs, N. Chopra, G.A. Ozin, Adv. Funct. Mater. 14 (2004) 335.
[21] G.J.A.A. Soler-Illia, C. Sanchez, B. Lebeau, J. Patarin, Chem. Rev. 102 (2002) 4093.
[22] G.J.A.A. Soler-Illia, A. Louis, C. Sanchez, Chem. Mater. 14 (2002) 750.
[23] Y. Wang, X. Tang, L. Yin, W. Huang, Y.R. Hacochen, A. Gedanken, Adv. Mater. 12 (2000) 1183.
[24] H. Luo, C. Wang, Y. Yan, Chem. Mater. 15 (2003) 3841.
[25] L.Z. Zhang, J.C. Yu, Chem. Commun. (2003) 1942.
[26] Y. Yue, Z. Gao, Chem. Commun. (2000) 1755.
[27] J.C. Yu, L.Z. Zhang, J.G. Yu, Chem. Mater. 14 (2002) 4647.
[28] M. Andersson, L. Osterlund, S. Ljungstrom, A. Palmqvist, J. Phys. Chem. B 106 (2002) 10674.
[29] J.C. Yu, L. Wu, J. Lin, P.S. Li, Q. Li, Chem. Commun. (2003) 1552.
[30] M.M. Wu, G. Lin, D.H. Chen, G.G. Wang, D. He, S.H. Feng, R.R. Xu, Chem. Mater. 14 (2002) 1974.
[31] J. He, W. Ma, J. He, J. Zhao, J.C. Yu, Appl. Catal. B: Environmental 39 (2002) 211.
[32] K. Vinodgopal, P.V. Kamat, Environ. Sci. Technol. 29 (1995) 841.
[33] K. Vinodgopal, P.V. Kamat, J. Phys. Chem. 96 (1992) 5053.
[34] C. Nasr, K. Vinodgopal, L. Fisher, S. Hotchandani, A.K. Chattopadhyay, P.V. Kamat, J. Phys. Chem. 100 (1996) 8436.
[35] F. Zhang, J. Zhao, T. Shen, H. Hidaka, E. Pelizzetti, N. Serpone, Appl. Catal. B: Environmental 15 (1998) 147.
[36] G. Liu, T. Wu, J. Zhao, H. Hidaka, N. Serpone, Environ. Sci. Technol. 33 (1999) 2081.
[37] T. Wu, G. Liu, J. Zhao, H. Hidaka, N. Serpone, J. Phys. Chem. B 103 (1999) 4862.
[38] T. Wu, T. Lin, J. Zhao, H. Hidaka, N. Serpone, Environ. Sci. Technol. 33 (1999) 1379.
[39] J. Bandara, J. Kiwi, New J. Chem. 23 (1999) 717.
[40] L. Lucarelli, V. Nadtochenko, J. Kiwi, Langmuir 16 (2000) 1102.
[41] J. Bandara, J.A. Mielczarski, J. Kiwi, Langmuir 15 (1999) 7670.
[42] M. Stylidi, D.I. Kondarides, X.E. Verykios, Appl. Catal. B: Environmental 47 (2004) 189.
[43] J.G. Yu, J.C. Yu, M.K.P. Leung, W.K. Ho, B. Cheng, X.J. Zhao, J.C. Zhao, J. Catal. 217 (2003) 69.
[44] J.C. Yu, L.Z. Zhang, J.G. Yu, New J. Chem. 26 (2002) 416.
[45] J.C. Yu, J.G. Yu, J.C. Zhao, Appl. Catal. B 36 (2002) 31.
[46] J.C. Yu, X.C. Wang, X.Z. Fu, Chem. Mater. 16 (2004) 1523.
[47] G. Busca, G. Ramis, J.M.G. Amores, V.S. Escribano, P. Piaggio, J. Chem. Soc. Faraday Trans. 90 (1994) 3181.
[48] A. Brioude, F. Lequevre, J. Mugnier, J. Dumas, G. Guiraud, J.C. Plenet, J. Appl. Phys. 88 (2000) 6187.
[49] D. Bersani, P.P. Lottici, X.Z. Ding, Appl. Phys. Lett. 72 (1998) 73.
[50] L. Wu, J.C. Yu, L.Z. Zhang, X.C. Wang, W.K. Ho, J. Solid State Chem. 177 (2004) 2584.
[51] Z. Ding, G.Q. Lu, P.F. Greenfield, J. Phys. Chem. B 104 (2000) 4815.
[52] D.R. Rolison, Science 299 (2003) 1698.
[53] T.R. Pauly, Y. Liu, T.J. Pinnavaia, S.T.L. Billinge, T.P. Rieker, J. Am. Chem. Soc. 121 (1999) 8835.
[54] R.T. Yang, T.J. Pinnavaia, W. Li, W. Zhang, J. Catal. 172 (1997) 488.
[55] J.F. Moulder, W.F. Stickle, P.E. Sobol, K.D. Bomben, Handbook of X-ray Photoelectron Spectroscopy, Perkin Elmer Corp., Eden Prairie, MN, 1992.
[56] J.C. Yu, J.G. Yu, H.Y. Tang, L.Z. Zhang, J. Mater. Chem. 12 (2002) 81.